

This is the accepted manuscript made available via CHORUS. The article has been published as:

Asymmetric excitation profiles in the resonance Raman response of armchair carbon nanotubes

Erik H. H  roz, Juan G. Duque, Eduardo B. Barros, Hagen Telg, Jeffrey R. Simpson, Angela R. Hight Walker, Constantine Y. Khripin, Jeffrey A. Fagan, Xiaomin Tu, Ming Zheng, Junichiro Kono, and Stephen K. Doorn

Phys. Rev. B **91**, 205446 — Published 29 May 2015

DOI: [10.1103/PhysRevB.91.205446](https://doi.org/10.1103/PhysRevB.91.205446)

Asymmetric Excitation Profiles in the Resonance Raman Response of Armchair Carbon Nanotubes

Erik H. H  roz,^{1,2} Juan G. Duque,³ Eduardo B. Barros,⁴ Hagen Telg,¹ Jeffrey R. Simpson,^{5,6} Angela R. Hight Walker,⁶ Constantine Y. Khripin,⁷ Jeffrey A. Fagan,⁷ Xiaomin Tu,⁷ Ming Zheng,⁷ Junichiro Kono,² and Stephen K. Doorn^{1,*}

¹*Center for Integrated Nanotechnologies, Los Alamos National Laboratory, Los Alamos, NM 87545, USA*

²*Department of Electrical and Computer Engineering, Rice University, Houston, TX 77005, USA*

³*Chemistry Division, Physical Chemistry and Applied Spectroscopy (C-PCS),
Los Alamos National Laboratory, Los Alamos, NM 87545, USA*

⁴*Laborat  rio de Microscopia Avan  ada, Universidade Federal do Cear  , Fortaleza-Cear  , Brasil*

⁵*Department of Physics, Astronomy, and Geosciences, Towson University, Towson, MD 21252, USA*

⁶*Semiconductor and Dimensional Metrology Division,
National Institute of Standards and Technology, Gaithersburg, MD 20899, USA*

⁷*Materials Science and Engineering Division, National Institute of Standards and Technology, Gaithersburg, MD 20899, USA*

We performed tunable resonance Raman spectroscopy on samples highly enriched in the (5,5), (6,6), (7,7), and (8,8) armchair structures of metallic single-wall carbon nanotubes. We present Raman excitation profiles (REPs) for both the radial breathing mode and G-band phonons of these species. G-band excitation profiles are shown to resolve the expected incoming and outgoing resonances of the scattering process. Notably, the profiles are highly asymmetric, with the higher-energy outgoing resonance weaker than the incoming resonance. These results are comparable to the asymmetric excitation profiles observed previously in semiconducting nanotubes, introduce a new electronic type, and broaden the structural range over which the asymmetry is found to exist. Modeling of the behavior with a third-order quantum model that accounts for the k -dependence in energies and matrix elements, without including excitonic effects, is found to be insufficient for reproducing the observed asymmetry. We introduce an alternative fifth-order model in which the REP asymmetry arises from quantum interference introduced by phonon-mediated state-mixing between the E_{11}^M and K -momentum excitons. Such state-mixing effectively introduces a nuclear coordinate dependence in the transition dipole moment and thus may be viewed as a non-Condon effect from a molecular perspective. This result unifies a molecular-like picture of nanotube transitions (introduced by their excitonic nature) with a condensed matter approach for describing their behavior.

PACS numbers: 78.67.Ch, 73.22.-f, 78.30.Na

I. INTRODUCTION

The graphene lattice serves as the underlying basis for the properties of both metallic and semiconducting single-wall carbon nanotubes (SWCNTs)¹. However, pronounced differences in the transport, optical, and in particular, the electron-phonon coupling behaviors of these two broad classes of nanotube electronic types arise from how the peculiarities of quantum confinement pair with the range of possible SWCNT structures to determine allowed electron wavevectors. Near the K -point of the Brillouin zone in metallic SWCNTs, the fundamental separability of electron and phonon wavefunctions, the Born-Oppenheimer approximation (BOA), breaks down². Other unique electron-phonon coupling processes for metallic SWCNTs include Peierls distortions³ and such non-adiabatic effects as the Kohn anomaly⁴ and related strong coupling of phonons to low-energy excitations of massless electrons between linear bands near the K -point⁵. For higher energy excitation away from the K -point, however, non-adiabatic effects play less of a role⁶, and the behavior of metallic optical transitions, now originating in higher-lying hyperbolic bands⁷, becomes similar to that observed in semiconducting SWC-

NTs. Of particular interest is the recent suggestion that for semiconducting SWCNTs the specific limiting case of BOA in which the optical transition dipole is considered to be independent of nuclear coordinates (the Condon approximation) fails⁸.

Introduction of such a coordinate dependence is found to give a clear spectroscopic signature: a strong asymmetry is introduced into the nanotube resonance Raman excitation profile (REP)⁸. In nanotube Raman scattering, resonance with the nanotube optical transitions can be met with either the incident excitation photon (incoming resonance), or with the inelastically scattered photon (outgoing resonance), with the expectation that two peaks corresponding to the two resonances will then be observed in the excitation profile. In the limit of the Condon approximation, the two peaks will have equal intensity^{8,9} and modeling of excitation profiles within this expectation has been standard practice in SWCNT resonance Raman spectroscopy^{10,11}. We have recently demonstrated for semiconducting SWCNTs, however, that the outgoing resonance is significantly weaker⁸. Because of similarities in the excitonic optical transitions of semiconducting and metallic species^{12–15} and differences in their electron-phonon couplings, it remains an impor-

tant and logical next step to establish if this asymmetry in the REPs also extends to metallic tubes. Furthermore, the physical origin of the effect in SWCNTs remains an open question, which in part may be addressed by evaluating the importance of certain symmetry directions within the Brillouin zone in determining the magnitude of the asymmetry. In this regard, results on semiconducting SWCNTs are suggestive of a larger asymmetry for species with a high chiral angle (θ)⁸, however, clear patterns in the structural dependence of the effects (present in other optical behaviors)^{1,16}, have yet to emerge. Evaluating the REP asymmetry over a broader structural range that encompasses even larger chiral angles is thus needed, making assessment for armchair metallic structures [chiral indices (n,m) having $n = m$ with $\theta = 30^\circ$] especially important.

Discussion of the REP asymmetry in terms of non-Condon effects borrows concepts from molecular spectroscopy that are motivated by the discrete and localized nature of the nanotube excitonic transitions. Such a perspective, however, represents a challenge for modeling within an extended condensed matter framework more typically applied to carbon nanotubes. Moura *et al.*¹⁷ recently demonstrated that the REP asymmetry can be reproduced for some semiconducting structures within such a view, without the need to invoke non-Condon effects, by applying a third-order quantum model for Raman scattering. The model captures the nanotube band structure by summing over the full range of momentum (k) states and includes the k -state dependence of energies and electron-phonon coupling. However, this model is problematic in that it neglects the excitonic nature of the optical transitions, which limits the relevant photoexcited states to excitons with a center-of-mass momentum close to zero, thus near the Γ -point of the Brillouin zone¹⁸. The symmetric shape of the band structure in this region can only yield symmetric REPs (see following discussion). Nonetheless, the results underscore the need for developing a condensed matter approach that advances our understanding of the origins of the REP asymmetry. A fruitful route towards unifying both perspectives may be found in recognizing that non-Condon effects often arise via phonon-mediated mixing of states, which can be modeled within tight-binding approaches.

Examining Condon versus non-Condon behaviors requires resonance Raman excitation profiles (REPs) from samples that are highly enriched in single chiralities so that the resonance responses from different species do not overlap and obscure the intrinsic asymmetry of the excitation spectrum. This is now possible for specific metallic species as a result of recent advances in separation techniques that yield samples enriched in armchair structures^{19–21}. Here, we present resonance Raman excitation spectra for the radial breathing mode (RBM) and G-band phonons for the (5,5), (6,6), (7,7), and (8,8) armchair nanotubes. The high-frequency ($\sim 1580 \text{ cm}^{-1}$) G-band allowed us to resolve the incoming and outgoing resonance peaks in the excitation profile. We un-

ambiguously demonstrate that the outgoing resonance is significantly weaker than the incoming resonance for each armchair structure, indicating that the REP asymmetries are as significant for metallic structures as they are in semiconducting nanotubes. Furthermore, we apply the approach of Moura *et al.*¹⁷ to the armchair data and find it is unable to reproduce the observed asymmetries. We present an alternative tight-binding approach that successfully reproduces the REP asymmetries by capturing non-Condon effects as a consequence of phonon-mediated state-mixing.

II. EXPERIMENTAL DETAILS

Samples highly enriched in the (6,6) and (7,7) armchair structures were obtained by DNA-based ion-exchange chromatography of CoMoCAT SG65 source material, as previously reported²⁰. Additionally, enrichment of the (5,5) (from CoMoCAT SG65EX source material) and (8,8) (from Rice-produced HiPco 107.1r source material) structures was provided via the recently introduced aqueous two-phase extraction technique (ATPE)^{21–23}. Complementary results obtained on samples enriched from HiPco source material (batch HPR 189.2) using a density gradient ultracentrifugation (DGU) approach^{19,24} are presented in the supporting material²⁵. In all cases, extensive ultrasonication during processing prior to separation generates samples that are predominantly water-filled. The absorption spectra of the (5,5) through (8,8) samples (Fig. 1) show each to be highly enriched in its respective single chirality. The absorption features of Fig. 1 correspond to the lowest energy optical transition (E_{11}^M) for each structure, with the experimentally obtained energies given in Table I.

Resonance Raman spectroscopy was performed using argon-ion, frequency-doubled Ti:Sapphire and dye (Rhodamine 560 and Coumarin 521 dyes) lasers to provide excitation energies from 2.19 to 3.30 eV, with 20 mW of incident power. Raman scattered light was collected from macroscopic samples in a backscattering geometry, dispersed in a triple monochromator, and detected on a UV-sensitive charge-coupled device (CCD) detector with two to five min. integration times. Spectra were calibrated for Raman shift using 4-acetamidophenol as a frequency standard and intensity-corrected for instrument response using benzonitrile as an intensity reference⁸.

III. RESULTS AND DISCUSSION

Raman spectra of the RBM region, taken with excitation near the peak of the E_{11}^M transition, for the four armchair species are shown in Fig. 2 (a). With the exception of the (8,8) sample, the spectra are remarkably clean, showing only the RBM feature for the isolated armchair chiralities. The (8,8) shows a small level of (10,4) contamination (RBM feature at 236 cm^{-1}). Absence of ad-

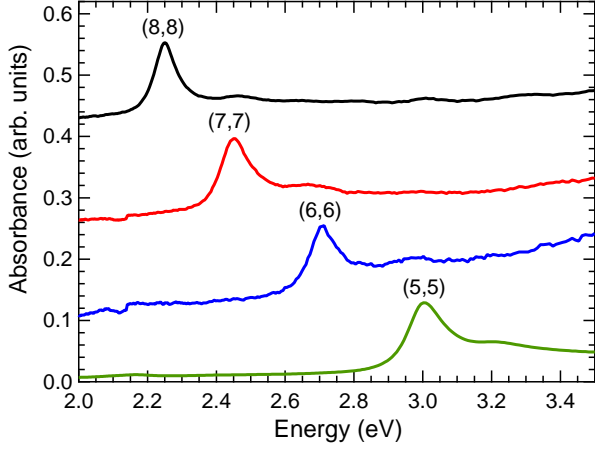


FIG. 1. Absorption spectra of the four samples used for resonance Raman measurements. The black, red, blue, and green traces are enriched in (8,8), (7,7), (6,6), and (5,5), respectively. The (7,7) and (6,6) samples were enriched by DNA-based ion-exchange chromatography²⁰ and the (8,8) and (5,5) samples were enriched by aqueous two-phase extraction²¹.

ditional RBM features from impurity chiralities is also true throughout the excitation range used to probe the armchair REPs, further indicating the high degree of enrichment of these species for each sample. The RBM frequencies found for the (8,8), (7,7), and (6,6), are 219, 248, and 287 cm^{-1} , respectively and match those found in previous work^{7,19,20,26,27}. The (5,5) RBM frequency is found here to be 338 cm^{-1} . The observed frequencies are fit well by the typical empirical relation relating the frequency (ω_{RBM}) to the tube diameter, d_t , such that $\omega_{\text{RBM}} = A/d_t + B$, with A and B given as $216 \pm 4 \text{ cm}^{-1} \text{ nm}$ and $21 \pm 4 \text{ cm}^{-1}$, respectively^{26,27}.

REPs showing the RBM intensity as it varies with the laser excitation energy for the four armchair species are shown in Fig. 2 (b). The REPs may be fit to Eq. 1, with Raman intensity I_{RRS}

$$I_{\text{RRS}} \propto \left| \frac{M_1}{E_L - E_{11}^M - i\frac{\Gamma}{2}} + \frac{M_2}{E_L - E_{11}^M - E_{ph} - i\frac{\Gamma}{2}} \right|^2 \quad (1)$$

dependent on laser excitation, optical transition, and phonon energies (E_L , E_{11}^M , E_{ph} , respectively), and an electronic broadening term Γ . The incoming and outgoing resonances discussed above are represented by the first and second terms in Eq. 1, respectively. In Eq. 1, M_1 and M_2 include the matrix elements for both the absorption and emission processes of the exciton-photon interaction, as well as for the exciton-phonon coupling. In fitting the experimental RBM data to Eq. 1, E_{ph} was fixed at the experimentally measured phonon frequency and $M_1 = -M_2$. The E_{ii} and Γ values obtained via the fitting procedure are given in Table I, with the E_{ii} extracted from the REP data agreeing with the position of the absorption maxima of Fig. 1. Finally, we note that

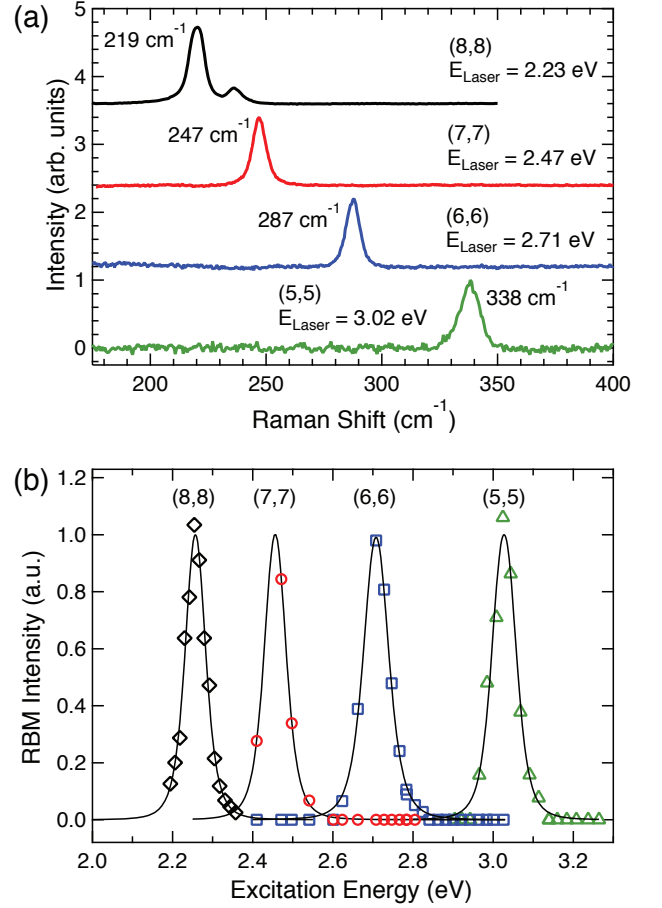


FIG. 2. (a) RBM Raman spectra of (8,8) [black, excitation at 2.23 eV], (7,7) [red, excitation at 2.47 eV], (6,6) [blue, excitation at 2.71 eV], and (5,5) [green, excitation at 3.02 eV]. (b) RBM resonance Raman excitation profiles of (8,8) [black diamonds], (7,7) [red circles], (6,6) [blue squares], and (5,5) [green triangles]. Solid traces are fits to the experimental data points using Eq. 1.

the REP Γ values of 80-100 meV (Table I), combined with the relatively low frequency of the RBM, prevent resolution of the incoming and outgoing resonances. Resolution requires accessing higher frequency modes, such as the G-band.

Raman spectra from which the G-band REPs are extracted are shown for all four armchair species in Fig. 3. Only a single peak is observed in each of the spectra, which is attributed to the transverse optical (TO) phonon²⁸. This observation holds for the full set of armchairs studied here (see Fig. 4 insets). This is a general result for all armchair nanotubes²⁸, for which the longitudinal optical (LO) phonon is not Raman-active due to symmetry^{29,30}. REPs for all structures are shown in Fig. 4. Two peaks in the REPs are observed for each of the armchair chiralities and define the incoming (lower energy peak) and outgoing (higher energy peak) resonances. The spacing of the two peaks is that of the

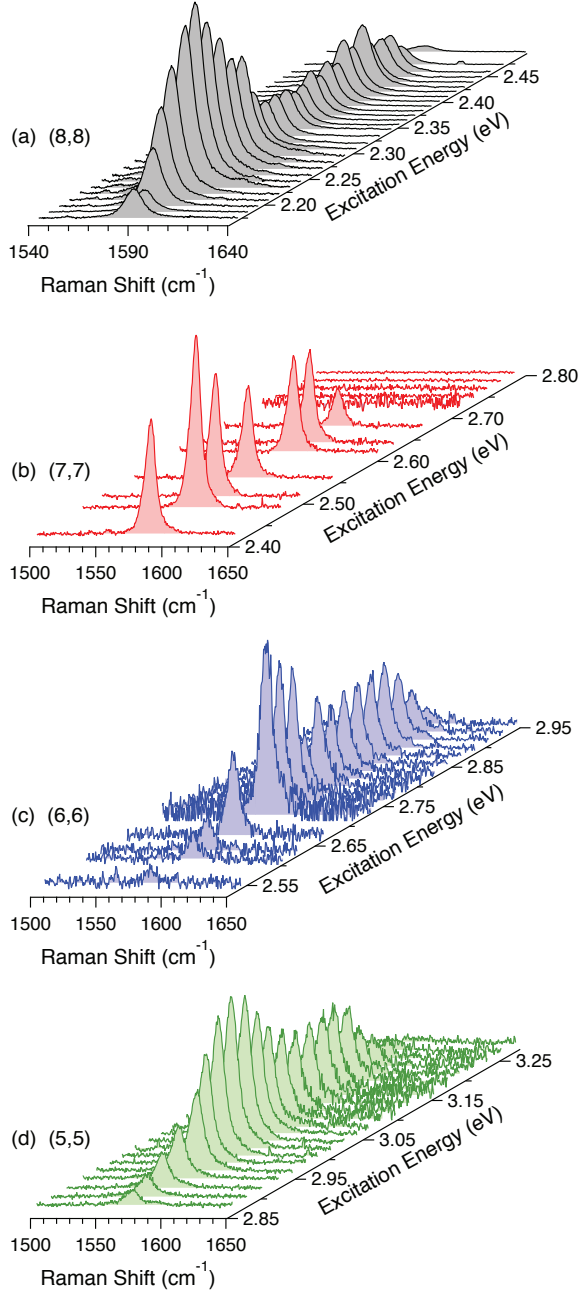


FIG. 3. Baseline-subtracted, G-band spectra for (a) (8,8) obtained at excitation from 2.16 to 2.5 eV; (b) (7,7) obtained at excitation from 2.41 to 2.8 eV; (c) (6,6) obtained at excitation from 2.55 to 2.92 eV; and (d) (5,5) obtained at excitation from 2.86 to 3.28 eV, with intensities corrected for instrument response.

TO phonon energy (~ 195 meV). The TO frequencies are 1573, 1581, 1586, and 1588 cm^{-1} for the (5,5), (6,6), (7,7), and (8,8) structures, respectively (see also Ref. 31).

As was previously found for semiconducting SWCNTs⁸, a pronounced asymmetry is observed in the TO REPs shown in Fig. 4 for each armchair structure, with the outgoing resonance showing significantly

weaker intensity than the incoming resonance. We find that this asymmetry is also independent of the SWCNT source material or the sample processing and separation methods. Results are similar for both the CoMoCAT and HiPco source materials, regardless of enrichment approach (DNA-based ion-exchange chromatography, density gradient ultracentrifugation, or ATPE)²⁵. The similarity of the asymmetric REP response found for both metallic and semiconducting species, paired with our finding here that the asymmetric REP is independent of SWCNT processing and source material provides further support that it is an intrinsic phenomenon. Previous indications of the intrinsic nature were founded primarily on theoretical considerations⁸.

In the following discussion, we first present an analysis of the armchair REP asymmetries in terms of the non-Condon interpretation originally put forth as the origin of the asymmetric REPs found for semiconducting structures⁸. Such a picture provides a useful basis for quantifying the magnitudes of the observed REP asymmetries. Next, we apply the third-order Raman analysis of Moura *et al.*¹⁷ and demonstrate that it is insufficient for modeling the observed asymmetries in the armchair data. We finish with a description of how the non-Condon model may be translated to a condensed-matter formalism in which phonon-mediated mixing of excitonic states is shown to be a viable route for introducing the asymmetric behavior.

A. Non-Condon Interpretation of REP Asymmetries

The localized nature of excitonic transitions in SWCNTs motivated the use of a molecular picture as a basis for describing the REP asymmetries arising as a consequence of non-Condon effects⁸. In the limit of validity of the Condon approximation, the incoming and outgoing resonance peaks would be of equal intensity, *i.e.*, $|M_1| = |M_2|$ in Eq. 1. It is clear from Fig. 4 that this is not the case for the G-band REPs. Our previous work on semiconducting structures⁸ demonstrated that the ob-

TABLE I. Fitting analysis of resonance Raman excitation profiles. First optical transition energies, E_{11}^M , were extracted from absorption (Abs.), RBM REP (RBM), and G-band TO REP (TO) data. The associated electronic broadening terms, Γ , were also extracted from RBM and G-band TO REP data. The non-Condon parameters (C , see Eq. 4) were extracted from G-band TO REP fits.

(n,n)	E_{11}^M (eV)			Γ (eV)		C
	Abs.	RBM	TO	RBM	TO	
(8,8)	2.252	2.243	2.239	0.083	0.071	0.32
(7,7)	2.453	2.441	2.441	0.086	0.099	0.23
(6,6)	2.709	2.690	2.701	0.098	0.099	0.20
(5,5)	3.008	3.007	2.990	0.084	0.118	0.23

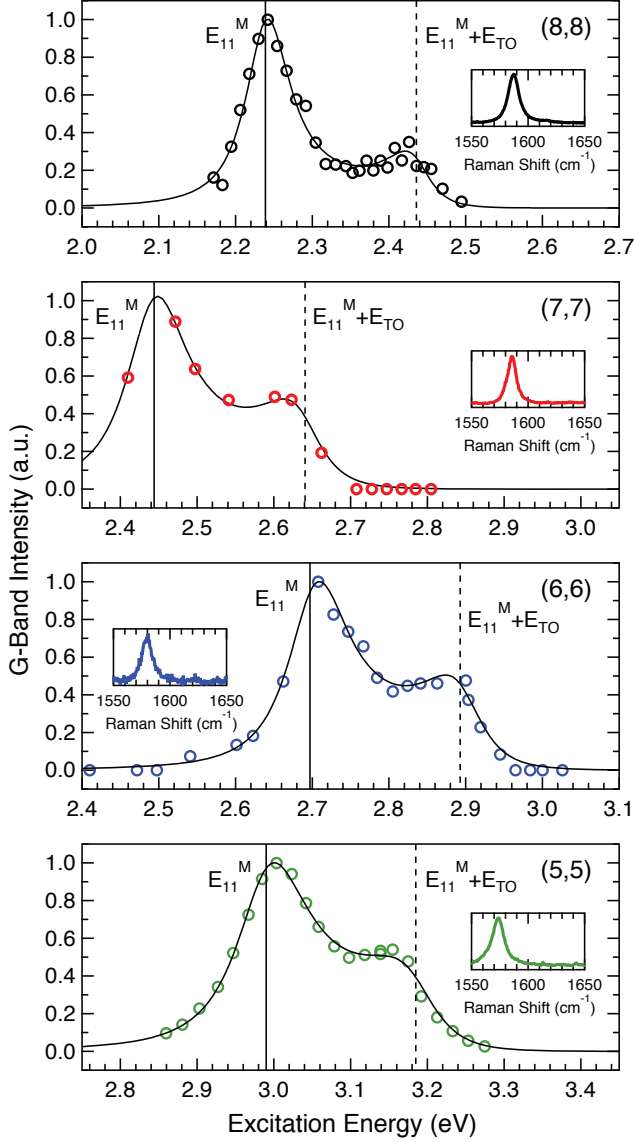


FIG. 4. G-band resonance Raman excitation profiles (intensities corrected for instrument response) for (8,8) [black circles], (7,7) [red circles], (6,6) [blue circles], and (5,5) [green circles]. Solid lines for (8,8), (7,7), (6,6), and (5,5) are empirical fits to Eq. 1 incorporating non-Condon effects (non-Condon parameter $C = 0.32, 0.23, 0.20$, and 0.23 , respectively; see Eq. 4). Vertical lines mark the position of the incoming (E_{11}^M , solid line) and outgoing ($E_{11}^M + E_{TO}$, dashed line) resonances. A representative G-band spectrum for each chirality is shown as an inset.

served REP asymmetry can be understood as a signature of a violation of the Condon approximation⁸. These non-Condon effects are defined as arising from the occurrence of a nuclear coordinate dependence in the transition dipole, which can be introduced into Eq. 1 as follows: Eq. 1 is ultimately derived from the Kramers-Heisenberg description of Raman scattering, with the Raman polar-

izability (α), given as

$$\alpha_{\rho\sigma} = \sum_{\nu} \left[\frac{\langle f | \mu_{\rho} | \nu \rangle \langle \nu | \mu_{\sigma} | g \rangle}{E_{\nu} - E_g - E_L - i\frac{\Gamma}{2}} + NR \right]. \quad (2)$$

Here, the initial $|g\rangle$, final $|f\rangle$, and intermediate states $|\nu\rangle$ of energies E_g , E_f , and E_{ν} , include both electronic and vibrational contributions. NR refers to nonresonant terms, which are neglected for our resonance excitation conditions. Separability of the electronic and vibrational degrees of freedom within the Born-Oppenheimer approximation allows the numerator in Eq. 2 to be expressed as the product of the exciton-phonon and the square of the exciton-photon coupling elements, as described for Eq. 1, with Raman intensity being proportional to the square of the polarizability. A nuclear coordinate dependence can be introduced into the transition dipole by expanding the transition dipole operator (μ) in a Taylor series of the nuclear coordinate (Q) of the phonon mode of interest: $\mu = \mu_0 + (\partial\mu/\partial Q)_0 Q$ ^{8,9,32}. The Raman polarizability (α) then becomes the sum of Condon (\mathcal{A}) and non-Condon (\mathcal{B}) contributions: $\alpha = \mathcal{A} + \mathcal{B}$. The \mathcal{A} -term scattering arises from the zeroth-order dipole contribution (μ_0), while the \mathcal{B} -term is introduced into Eq. 2 by the second term of the dipole expansion^{9,32}. Depending on the relative sign and magnitude of the \mathcal{A} - and \mathcal{B} -terms, the two contributions can interfere constructively or destructively. Since the Raman intensity is dependent on the square of the polarizability, the asymmetry observed in the TO REPs may be interpreted as an interference effect between the Condon and non-Condon contributions. This is different than the more commonly considered interference that may occur in Raman scattering when excitation is with two closely-spaced electronic transitions³³.

In the absence of non-Condon (\mathcal{B} -term) contributions, the Condon (\mathcal{A} -term) by itself directly yields Eq. 1 with $|M_1| = |M_2|$. Non-Condon contributions to the REP may be incorporated into Eq. 1 by first defining a non-Condon parameter C , that is a relative measure of the sensitivity of the transition dipole to changes in nuclear coordinate:

$$C = [(\partial\mu/\partial Q)_0/\mu_0] \times (1/2S)^{1/2}. \quad (3)$$

The Huang-Rhys factor is defined as $S = \Delta^2/2$, with Δ being the excited-state displacement along the phonon normal mode coordinate^{8,9,32}. The relation

$$C = \frac{(M_1 + M_2)}{(M_1 - M_2)} \quad (4)$$

has been demonstrated as a simple means for introducing non-Condon effects into Eq. 1⁸. A nonzero value of C makes M_1 and M_2 unequal, with the result being the observed weaker intensity of the outgoing resonance (effectively appearing as a destructive interference in the response).

By using this result in Eq. 1, we are able to account for the non-Condon effects in fitting the TO REPs for all four armchair species (Fig. 4). Excellent fits to the experimental intensities are found, with E_{ph} in this case fixed

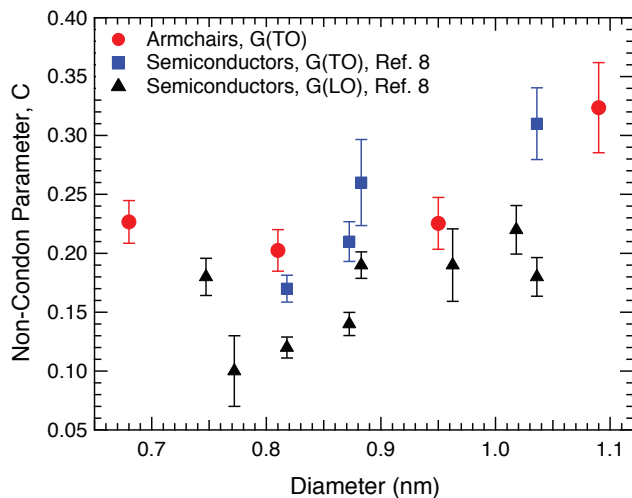


FIG. 5. Plot of non-Condon parameter, C , for specific SWCNT species as a function of nanotube diameter. Semiconductor LO and TO C -values were taken from Ref. 8 while armchair TO values were taken from this work. Error bars were calculated by standard error propagation of M_1 and M_2 fitting uncertainties.

to the experimentally observed TO frequencies. The values obtained for E_{11}^M and Γ agree well with those obtained from fitting to the RBM REPs (Table I). The fits also allow determination of C , with values of 0.23, 0.20, 0.23, and 0.32 for the (5,5), (6,6), (7,7), and (8,8) structures, respectively (see Table I). In contrast to the asymmetry of the G-band REPs, neglecting the non-Condon effects in fitting the RBM REPs of Fig. 2 (*i.e.*, assuming $C = 0$) does not impact the quality of the fits. This is a result of the inability to resolve the two resonance peaks in the RBM REPs.

In Figure 5, we plot the C values for the TO phonons of the armchair structures along with those previously found for the semiconducting TO and LO phonons. We find that the C -parameter values for armchair nanotubes track closely with those found for semiconducting nanotubes of a similar diameter, particularly when a direct comparison is made between the TO phonon behavior of the armchair and semiconducting structures. In particular, in our work on semiconducting species⁸, a weak dependence of the non-Condon behavior on nanotube diameter (d_t) was found, such that C increases with d_t . Especially when considered collectively with the semiconducting data (Fig. 5), the armchair C values appear to continue the trend evident in semiconducting structures.

The chiral angle (θ) dependence of the behavior is not yet clear, but again the armchair results provide interesting comparisons to semiconducting tubes. When the semiconductor and metallic data are combined, behaviors at a specific diameter begin to suggest that high-chiral-angle species may show the largest C values and that near-armchair structures may represent an upper limit to the asymmetry at a given tube diameter. For

example, the C -parameter value for the (6,6) species ($d_t = 0.814$ nm) is a close match to that for the (7,5) structure, with $d_t = 0.818$ nm and $C_{TO} = 0.17$ ⁸. We note that near-armchair species such as the (7,5) and (8,7) structures tend to show larger C values within their $2n+m = \text{constant}$ families⁸. The range of data available, however, is as yet insufficient to make any strong claims in this regard. This is an important issue to resolve in future studies in that optical behavior of armchair structures have commonly served as a reference point for chiral dependence of both absorption and emission behaviors¹⁶ and for trends in radial breathing mode frequencies and intensities^{1,18,34}.

The parallel asymmetric REP response observed for semiconducting and armchair metallic SWCNTs emphasizes the similar nature of their optical excitations. Indeed, the fact that the armchair REP lineshapes are well-described by Eq. 1 (with non-Condon contributions properly accounted for) indicates that the two resonances are determined primarily by the main excitonic feature of the absorption spectrum. While the semiconducting and armchair REPs are found here to show parallel behaviors, in the metallic structures there exists the possibility for perturbation of this behavior via the damping and screening influence of massless electrons at the Fermi level in the linear bands that cross at the K -point, a feature not present in the semiconducting chiralities. For symmetry reasons, the TO phonon does not couple to these bands⁵, and therefore it is not surprising that the influence of the linear bands is not apparent in the response shown in Fig. 4. The potential to explore the possible influence of the linear bands, however, exists through probing the resonance Raman response of the LO mode, which is Raman-active in non-armchair metallic structures²⁹. Significant alteration of the asymmetric REP behavior of the LO phonon in such structures may be expected due to its ability to strongly couple to low-energy excitations within the linear bands⁵. Such a possibility provides motivation for the isolation of enriched samples of non-armchair metallic chiralities for follow-up studies.

B. Evaluation of Third-Order, non-Excitonic, Quantum Model for Raman Scattering

While the molecular picture of the asymmetric REPs arising as a non-Condon effect proves useful as a basis for quantitative analysis of the asymmetry and in providing an initial basis for the origins of the effect, the model falls short in providing an understanding of potential chirality dependences (d_t and θ) of the behavior. The origins of chirality-dependent behavior in other SWCNT optical processes typically arise from where in the Brillouin zone the relevant transitions originate. Such details can be modeled effectively by applying condensed-matter approaches based in tight-binding models. We begin here a comparison of two such potential approaches. The first is an application to our data of the third-order, non-

excitonic description put forward by Moura *et al.*¹⁷. The second incorporates non-Condon effects into a condensed matter formalism via the introduction of a state-mixing description.

In recent work¹⁷, experimentally measured REPs for the (6,5) and (7,5) nanotubes could be well-reproduced by considering the contribution to the Raman scattering process of all possible electron-hole states throughout the Brillouin zone. This model is based on a third-order time-dependent perturbation theory description for the Raman process³⁵, for which the G-band Raman intensity (I_G) is given by

$$I_G = E_L(E_L - \hbar\omega_G)^3 \frac{1}{N_k^2} \times \left| \sum_k \frac{M_k^{ept} M_{k,k}^{eph} M_k^{ept}}{[E_L + \hbar\omega_G - \Delta E(k) + i\frac{\Gamma}{2}][E_L - \Delta E(k) + i\frac{\Gamma}{2}]} \right|^2, \quad (5)$$

where M^{ept} and M^{eph} represent the matrix elements for the electron-photon and electron-phonon interactions, respectively. E_L is the laser excitation energy, $\Delta E(k)$ is the energy separation between the valence and conduction bands, ω_G is the G-band phonon frequency and Γ is the broadening factor associated with the excitation lifetime. Moura *et al.* argued that in order to reproduce the experimentally observed asymmetry in the REPs it is necessary to perform the sum in Eq. 5 for all possible values of k in the nanotube Brillouin zone, thus requiring a detailed knowledge of the matrix elements and how they vary throughout the nanotube reciprocal space¹⁷.

This model has two important advantages: first is its capacity to reproduce qualitatively the experimental results, including the weak diameter dependence of the REP asymmetry we observe²⁵. The second is its simplicity, which allows for a straightforward calculation as long as the relevant matrix elements can be accurately determined.

A significant shortcoming of this model lies in that it is theoretically incompatible with the strongly bound excitonic description of the optical excitations in carbon nanotubes. For strongly bound excitons, the exciton-photon matrix element is only non-zero for excitonic states with a wavevector Q near the Γ -point¹⁸. Therefore, the integration along the Brillouin zone should be substituted by a sum of discrete $Q = 0$ excitonic states. Furthermore, the oscillator strength for strongly bound excitons is mainly located at the lowest lying optically active state. Thus, only one excitonic state contributes to the Raman scattering process. Within this approximation, the REPs for all nanotubes should be strictly symmetric. Furthermore, in order to perform a reliable calculation of the electron-phonon matrix elements it is necessary to have a formal knowledge of the phonon polarization for each nanotube, a problem that has been the subject of intense discussion in the literature and for which no final conclusion has been reached. In this sense, it is not yet well estab-

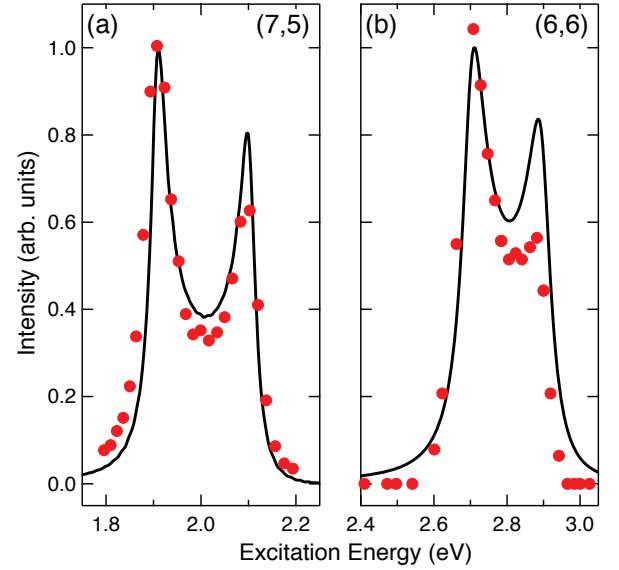


FIG. 6. Experimental (red dots) and theoretical (solid lines) Raman excitation profiles for (a) the LO mode of (7,5) semi-conducting nanotubes (REP data taken from Ref. 8) and (b) the TO mode of (6,6) armchair nanotubes. The theoretical calculations were performed using a simple tight-binding approach, as per Moura *et al.*¹⁷.

lished if the phonon responsible for the G^+ (G^-) bands for a chiral nanotube is polarized along the nanotube axis (circumference) or along some other direction.

With this in mind, the armchair carbon nanotubes studied in this work stand as a perfect sample for testing the validity of the third-order model. First, the screening effects expected for these metallic nanotubes weaken the electron-hole interaction, leading to more weakly bound excitons, for which this model could in principle be valid. Also, in these achiral nanotubes it is well established that the G-band Raman is composed of a single peak corresponding to the TO phonon mode (polarized along the nanotube circumferential direction)^{7,28}. In fact, it has been shown that for these nanotubes the electron-phonon matrix elements for phonons polarized along the axial direction have negligible intensity³⁰, and therefore, even if the phonon were to be polarized along an arbitrary direction along the nanotube surface, only the projection of the atomic displacements along the nanotube circumferential direction can contribute to the electron-phonon interaction. Therefore, the REPs for armchair nanotubes can be calculated unambiguously allowing for a direct comparison with experiments.

To this end, we reproduced the approach of Moura *et al.*¹⁷ using a simple tight-binding model for calculating the electronic bands of graphene, together with a zone-folding scheme for obtaining the electronic bands of the selected carbon nanotubes. The electron-phonon and electron-photon coupling matrix elements were also calculated within a tight-binding model, but included the contribution of the 5 nearest neighbors and assuming

that both the phonon deformation potential and dipole transition vectors decrease exponentially with the interatomic distance. The phonon displacement for the G-band is considered to be directed along the circumferential direction of the nanotube for armchair nanotubes and along the longitudinal direction for the semiconducting nanotubes³⁶. The position of the calculated transition energy and the exciton lifetime were chosen in order to best fit the experimental results. We show in Fig. 6 a comparison between calculated and experimental REPs for a (7,5) semiconducting nanotube and for a (6,6) armchair nanotube. The REP of the (7,5) [Fig. 6 (a)] could be well-reproduced, as was previously shown by Moura *et al.*¹⁷. However, for the (6,6) structure [Fig. 6 (b)] the asymmetry for the calculated REP is much weaker than that observed experimentally. The same was found to be true for all the armchair nanotubes studied here (see Fig. 8). This discrepancy in the model of Moura *et al.* probably arises from the fact that for the armchair nanotubes there is a large energy difference between the electronic bands, thus decreasing the interference between the contributions from these different bands that otherwise would have increased the calculated asymmetry.

C. Fifth-Order Raman Processes

The shortcomings of the molecular and third-order solid-state models presented in sections III A and III B, respectively, highlight the need to reconcile the two viewpoints within a unified description that captures the dual behavior of molecular-like excitonic transitions arising from the extended SWCNT structure. In order to describe the REP asymmetries within a condensed matter formalism that also captures the excitonic nature of the optical excitations in carbon nanotubes, we propose a fifth-order time-dependent perturbation theory approach for describing REPs, in which the non-Condon effects are taken into account implicitly. The Raman scattering process is usually described in terms of a third-order time-dependent perturbation theory approach. For systems in which the optical excitations are governed by excitonic effects, the Raman scattering process can be depicted by the third-order Feynman diagram shown in Fig. 7. In principle, higher-order terms can contribute to the Raman scattering process. However, for materials in which the exciton-phonon interactions are weak, the higher-order terms can be readily disregarded and up to third-order terms are sufficient for describing their Raman excitation profile.

The absorption spectra of carbon nanotubes are populated by phonon sidebands^{36,37}. The most prominent of these absorption sidebands is a peak positioned at around 0.210 eV above each of the main absorption peaks and which are usually associated with a K -point phonon-related indirect absorption^{38,39}. The presence of this peak suggests that, for the case of carbon nanotubes, the exciton-phonon interaction is strong enough that the

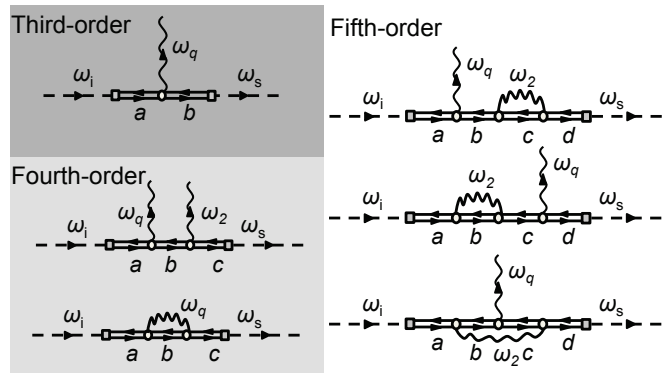


FIG. 7. Possible Feynman Diagrams for third-order (top left), fourth-order (bottom left), and fifth-order (right) scattering processes. Dashed lines represent the incident (ω_i) and scattered (ω_s) photons, the wavy lines represent phonon states (in this case, ω_2 is the mediating K -point phonon and ω_q is the emitted G-band phonon), and the double lines represent intermediate excitonic states. Only third- and fifth-order processes can be related to one-photon Raman scattering. The a , b , c and d labels represent possible different excitonic states in each process.

higher-order contributions to the Raman process cannot be disregarded.

This indicates that for a complete description of the Raman scattering process in carbon nanotubes, higher-order terms in the perturbation series should also be considered. Below, we will show that considering the contribution of both the third-order and the fifth-order terms in the time-dependent perturbation theory expansion (shown in Fig. 7) will lead to an asymmetric line-shape consistent with the experimental results. This is analogous to the expansion of the transition dipole in Eq. 2 to introduce a nuclear coordinate dependence. It should be mentioned that the fourth-order processes can only contribute to Rayleigh scattering, and to the two-phonon Raman processes such as the one related to the G' -band. For this reason, only third-order and fifth-order processes will be considered.

For simplicity, we will consider that only two of the nanotube phonons have relevant matrix elements and thus can contribute to a Raman process: the G-band phonon, which is a totally symmetric phonon at the Γ -point of armchair nanotubes (A_{1g}) and with energy $\hbar\omega_G = 0.197$ eV, and the TO phonon near the K -point, which is responsible for the D- and G' -bands and which contributes to the phonon-assisted absorption. We will assume the energy of this phonon to be given by $\hbar\omega_K = 0.163$ eV, independent of the nanotube diameter. For the excitons, we will also simplify the system by considering explicitly only two states in the manifold of excitonic states expected for each pair of electronic subbands, namely, we will consider the bright singlet exciton at the Γ -point ($B\Gamma S$) and the dark singlet state near the K -point (DKS). We will assume that the oscillator strength is concentrated in the bright exciton and

that the Γ -point phonon responsible for the G-band can only couple excitonic states with the same momentum while the K -point phonon exchanges the two excitons. In summary, the exciton-phonon interaction is simplified to

$$H_{XP} = M_G^{XP} [F_{B\Gamma S}^\dagger F_{B\Gamma S} + F_{DKS}^\dagger F_{DKS}] (b_G + b_G^\dagger) + M_K^{XP} [F_{B\Gamma S}^\dagger F_{DKS} + F_{DKS}^\dagger F_{B\Gamma S}] (b_K + b_K^\dagger), \quad (6)$$

and the exciton-photon interaction is simplified to

$$H_{XL} = \sum_{\omega} M_0^{XL} (F_{B\Gamma S} + F_{B\Gamma S}^\dagger) (a_{\omega} + a_{\omega}^\dagger). \quad (7)$$

In these equations, F_j^\dagger (F_j) corresponds to the creation (annihilation) of an exciton in state $j = B\Gamma S$ or DKS , b_q^\dagger (b_q) creates (annihilates) either a Γ -point optical phonon corresponding to the G-band ($q = G$) or a K -point phonon ($q = K$) and a_{ω}^\dagger (a_{ω}) creates (annihilates) a photon with energy $\hbar\omega$. M_{XP} and M_{XL} are exciton-phonon and exciton-photon matrix elements.

Within this simplified model, the G-band intensity as a function of the laser excitation energy (E_L) can be calculated to fifth-order as $I_{\text{Raman}} \propto |W_G|^2$, where

$$W_G = \frac{|M_{B\Gamma S}^{XL}|^2 M_G^{XP}}{(E_{B\Gamma S} + \hbar\omega_G - E_L)(E_{B\Gamma S} - E_L)} \times \left[1 + \frac{|M_G^{XP}|^2}{(E_{B\Gamma S} + 2\hbar\omega_G - E_L)(E_{B\Gamma S} + \hbar\omega_G - E_L)} + \frac{|M_G^{XP}|^2}{(E_{B\Gamma S} - E_L)(E_{B\Gamma S} + \hbar\omega_G - E_L)} + \frac{|M_K^{XP}|^2}{(E_{DKS} + \hbar\omega_K + \hbar\omega_G - E_L)(E_{B\Gamma S} + \hbar\omega_G - E_L)} + \frac{|M_K^{XP}|^2}{(E_{DKS} + \hbar\omega_K + \hbar\omega_G - E_L)(E_{DKS} + \hbar\omega_K - E_L)} + \frac{|M_K^{XP}|^2}{(E_{B\Gamma S} - E_L)(E_{DKS} + \hbar\omega_K - E_L)} \right] \quad (8)$$

The first term corresponds to the third-order term, whereas the other 5 terms correspond to the fifth-order contributions. The energies of the bright ($E_{B\Gamma S}$) and dark (E_{DKS}) excitons have both real and imaginary parts such that $E_{B\Gamma S} = E_{ii} + i\gamma_{\Gamma}/2$ and $E_{DKS} = E_K + i\gamma_K/2$, where the imaginary parts are associated with the excitonic lifetimes.

To better illustrate the energetics of fifth-order contributions to the Raman scattering process, we show in Fig. 8 (a) a schematic for one of the Raman processes mediated by the K -point phonon. In this particular process, the photoexcited $B\Gamma S$ exciton is scattered to the DKS exciton state by emitting a K -point phonon, then it is scattered back to the $B\Gamma S$ by re-absorbing the K -point phonon, and then it emits a G-band phonon before exciton recombination. This process is especially resonant

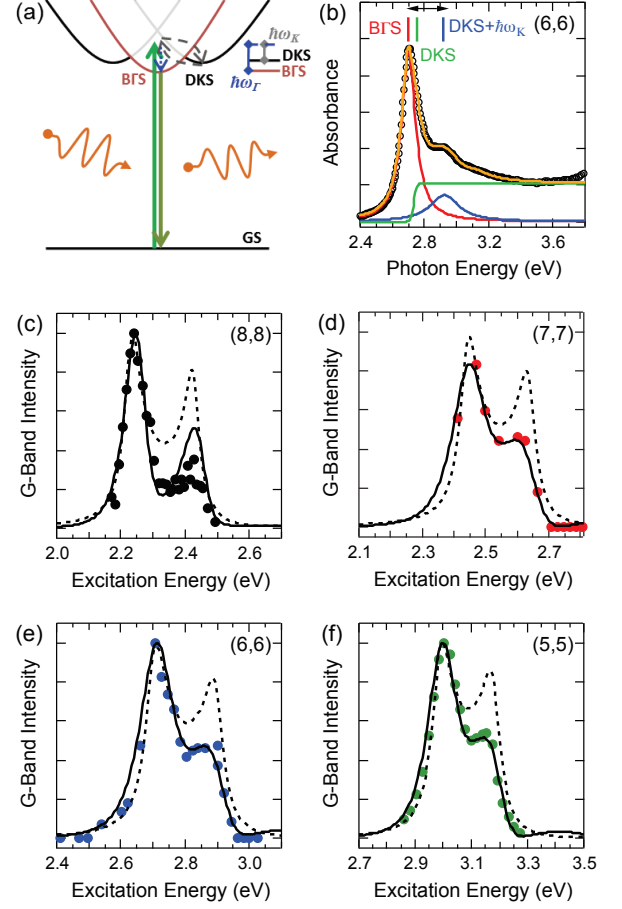


FIG. 8. (a) Schematic of one of the possible fifth-order G-band Raman processes involving the coupling with dark excitons through a K -point phonon; (b) Absorption spectra for the (6,6) nanotube fitted with different contributions. The black circles show the experimental results. The red line corresponds to direct absorption, the blue line corresponds to the phonon-assisted absorption peak and the green step function corresponds to the onset of the continuum states. Experimental REP for the (c) (5,5) (d) (6,6), (e) (7,7) (f) (8,8) nanotubes (solid circles) compared to the REP calculated using Eq. 8 (solid lines). Calculated REPs using the third-order model (Eq. 5) appear as dashed lines.

for $E_L = E_{B\Gamma S} + \hbar\omega_G \sim E_{DKS} + \hbar\omega_K$ but interferes destructively with the third-order process, leading to a magnitude decrease for the peak corresponding to the resonance with the scattered light and thus giving rise to the observed REP asymmetry.

To check the accuracy of this model, we fitted the measured REPs for the armchair nanotubes. The values for $E_{B\Gamma S}$ and E_{DKS} were extracted from the absorption spectra. The energy of the bright exciton is obtained as the position of the main peak [red line in Fig. 8(b)] while the energy of the dark exciton is obtained as $E_{DKS} = E_{SB} - \hbar\omega_K$, where E_{SB} is the energy position of the absorption sideband [blue line in Fig. 8(b)]⁴⁰. The best fit values for the $E_{B\Gamma S}$, E_{SB} ,

TABLE II. Energy values obtained for the $E_{B\Gamma S}$ exciton and for the exciton-phonon sideband E_{SB} and the calculated values for E_{DKS} and Δ_K from the optical absorption spectra (Energy values are in eV).

(n,m)	$E_{B\Gamma S}$	E_{SB}	E_{DKS}	Δ_K
(5,5)	3.00	3.23	3.07	0.07
(6,6)	2.70	2.92	2.76	0.06
(7,7)	2.45	2.69	2.53	0.08
(8,8)	2.25	2.48	2.32	0.07

E_{DKS} and $\Delta_K = E_{DKS} - E_{B\Gamma S}$ are shown in Table II.

The same set of parameters were used to fit all the studied armchair nanotubes: $|M_K^{XP}| = 0.13$ eV, $\gamma_T = 0.18$ eV, $\gamma_K = 0.26$ eV. The only exception is for the (8, 8) nanotube, which shows a REP with much sharper peaks, and thus the best fit was obtained with $\gamma_T = 0.12$ eV. The calculated REPs for the different nanotubes are in good agreement with the experimental results [Fig. 8 (c-f)], indicating that this model can successfully account for the asymmetric behavior of the Raman excitation profile in armchair carbon nanotubes. It is thus a promising model for describing the non-Condon nature of the Raman process in carbon nanotubes within a condensed matter framework.

It should be stressed here that in this work the excitonic nature of the optical transitions is taken into account simply by considering discrete excitonic states. We have not performed any detailed calculation of the exciton binding energies^{41,42} or of the exciton-phonon coupling matrix elements^{18,39}. Furthermore, for a complete description of the asymmetry within this model, knowledge of the exciton lifetimes is also necessary. While beyond the scope of this work, performing such calculations will provide a more definitive verification of the relevance of the fifth-order Raman process to the asymmetric REP lineshapes. In addition to incorporating non-Condon effects through phonon-mediated mixing of excitonic states, such an approach would capture the specific SWCNT band structure and the role of excitons by explicitly accounting for exciton dispersions. Nevertheless, our results provide a solid framework in which to carry out such calculations. There is precedence for such an approach in earlier work on GaAs quantum wells. Asymmetric REPs observed for GaAs systems were successfully modeled by accounting for phonon-mediated interaction between two or more discrete exciton states, with a complete description including band structure and the critical role of excitons by including exciton dispersions through k -space sampling⁴³⁻⁴⁵. While further refinements will be important, as presented our fifth-order model addresses the shortcomings of the molecular approach and that of Moura *et al.* by accounting for excitons as discrete states and in providing a physical origin for the observed asymmetries that may be applied generally for both metallic and semiconducting SWCNTs. Such generality further supports the assignment

of the absorption sideband in armchair SWCNTs as a K -momentum phonon sideband^{20,38,39,46}. This picture provides predictive capability for understanding relative differences in REP asymmetries that may be found for different phonons (RBM, TO, LO), which is the subject of ongoing work.

IV. CONCLUSION

In conclusion, the strong asymmetry found in the TO resonance Raman excitation profiles introduces another common link between the optical behaviors of metallic and semiconducting species. In all cases, the outgoing resonance peak is significantly weaker than that for the incoming resonance. This result is also a clear demonstration that significant REP asymmetries are a general and intrinsic behavior for all nanotube types. We note that in each of the three theoretical models, the REP asymmetry arises as a quantum interference effect. In the molecular interpretation, the interference occurs between the Condon and non-Condon contributions to the Raman polarizability. In the third-order model, it arises between different third-order processes originating at different points within the Brillouin zone. Finally, in the fifth-order model, interference arises between the third-order and fifth-order contributions to Eq. 8. The successful modeling of the armchair REP data with the fifth-order condensed-matter model via phonon-mediated state-mixing provides a connection to a molecular view of this asymmetry as a non-Condon effect. Therefore, the fifth-order model provides a framework within which the molecular and solid-state aspects of the SWCNT Raman response may be unified. The results demonstrate that the TO mode can efficiently mix excitonic states, effectively resulting in a nuclear coordinate dependence of the transition dipole when the process is viewed as intensity borrowing. The model further indicates that the excitonic nature of SWCNT optical transitions ultimately is at the heart of the asymmetric REP behavior. The fifth-order model presented here should form a fruitful basis for continued theoretical and experimental probing of this phenomenon.

ACKNOWLEDGMENTS

E.H.H., J.G.D., H.T. and S.K.D. acknowledge partial support from the LANL-LDRD program. E.H.H. and H.T. also gratefully acknowledge support from the LANL Director's Postdoctoral Fellowship. E.H.H. and J.K. were supported by the DOE/BES through Grant DEFG02-06ER46308 and the Robert A. Welch Foundation through Grant C-1509. E.B.B. acknowledges financial support from CNPq grants 470492/2012-0 and 245640/2012-6. X.T. and M.Z. acknowledge support from NSF Grant CMS-060950. We thank Anna Swan for helpful discussions. This work was performed in part at the

Center for Integrated Nanotechnologies, a U.S. Department of Energy, Office of Basic Energy Sciences user facility. Certain equipment, instruments or materials are identified in this paper in order to adequately specify the

experimental details. Such identification does not imply recommendation by the authors nor does it imply the materials are necessarily the best available for the purpose.

-
- * skdoorn@lanl.gov
- ¹ A. Jorio, G. Dresselhaus, and M. S. Dresselhaus, eds., *Carbon Nanotubes: Advanced Topics in the Synthesis, Structure, Properties and Applications*, Topics in Applied Physics, Vol. 111 (Springer, Heidelberg, 2008).
 - ² A. W. Bushmaker, V. V. Deshpande, S. Hsieh, M. W. Bockrath, and S. B. Cronin, *Nano Lett.* **9**, 2862 (2009).
 - ³ S. Piscanec, M. Lazzeri, J. Robertson, A. C. Ferrari, and F. Mauri, *Phys. Rev. B* **75**, 035427 (2007).
 - ⁴ O. Dubay, G. Kresse, and H. Kuzmany, *Phys. Rev. Lett.* **88**, 235506 (2002).
 - ⁵ M. Lazzeri, S. Piscanec, F. Mauri, A. C. Ferrari, and J. Robertson, *Phys. Rev. B* **73**, 155426 (2006).
 - ⁶ S. Pisana, M. Lazzeri, C. Casiraghi, K. S. Novoselov, A. K. Geim, A. C. Ferrari, and F. Mauri, *Nature Mat.* **6**, 198 (2007).
 - ⁷ E. H. H  roz, J. G. Duque, X. Tu, M. Zheng, A. R. H. Walker, R. H. Hauge, S. K. Doorn, and J. Kono, *Nanoscale* **5**, 1411 (2013).
 - ⁸ J. G. Duque, H. Chen, A. K. Swan, A. P. Shreve, S. Kilina, S. Tretiak, X. Tu, M. Zheng, and S. K. Doorn, *ACS Nano* **5**, 5233 (2011).
 - ⁹ R. Kumble, I. T. S. Rush, J. M. E. Blackwood, P. M. Kozlowski, and T. G. Spiro, *J. Phys. Chem. B* **102**, 7280 (1998).
 - ¹⁰ M. A. Pimenta, A. Marucci, S. A. Empedocles, M. G. Bawendi, E. B. Hanlon, A. M. Rao, P. C. Eklund, R. E. Smalley, G. Dresselhaus, and M. S. Dresselhaus, *Phys. Rev. B* **58**, R16016 (1998).
 - ¹¹ C. Thomsen and S. Reich, in *Light Scattering in Solids IX*, Topics in Applied Physics, Vol. 108 (Springer-Verlag, Berlin, 2007) pp. 115–235.
 - ¹² F. Wang, G. Dukovic, L. E. Brus, and T. F. Heinz, *Science* **308**, 838 (2005).
 - ¹³ F. Wang, D. J. Cho, B. Kessler, J. Deslippe, P. J. Schuck, S. G. Louie, A. Zettl, T. F. Heinz, and Y. R. Shen, *Phys. Rev. Lett.* **99**, 227401 (2007).
 - ¹⁴ S. K. Doorn, P. T. Araujo, K. Hata, and A. Jorio, *Phys. Rev. B* **78**, 165408 (2008).
 - ¹⁵ P. May, H. Telg, G. F. Zhong, J. Robertson, C. Thomsen, and J. Maultzsch, *Phys. Rev. B* **82**, 195412 (2010).
 - ¹⁶ S. M. Bachilo, M. S. Strano, C. Kittrell, R. H. Hauge, R. E. Smalley, and R. B. Weisman, *Science* **298**, 2361 (2002).
 - ¹⁷ L. G. Moura, M. V. O. Moutinho, P. Venezuela, C. Fantini, A. Righi, M. S. Strano, and M. A. Pimenta, *Phys. Rev. B* **89**, 035402 (2014).
 - ¹⁸ J. Jiang, R. Saito, K. Sato, J. S. Park, G. G. Samsonidze, A. Jorio, G. Dresselhaus, and M. S. Dresselhaus, *Phys. Rev. B* **75**, 035405 (2007).
 - ¹⁹ E. H. H  roz, W. D. Rice, B. Y. Lu, S. Ghosh, R. H. Hauge, R. B. Weisman, S. K. Doorn, and J. Kono, *ACS Nano* **4**, 1955 (2010).
 - ²⁰ X. Tu, A. R. Hight Walker, C. Y. Khripin, and M. Zheng, *J. Am. Chem. Soc.* **133**, 12998 (2011).
 - ²¹ J. A. Fagan, C. Y. Khripin, C. A. S. Batista, J. R. Simpson, E. H. H  roz, A. R. H. Walker, and M. Zheng, *Adv. Mater.* **26**, 2800 (2014).
 - ²² C. Y. Khripin, J. A. Fagan, and M. Zheng, *J. Am. Chem. Soc.* **135**, 6822 (2013).
 - ²³ N. K. Subbaiyan, S. Cambr  , A. N. G. Parra-Vasquez, E. H. H  roz, S. K. Doorn, and J. G. Duque, *ACS Nano* **8**, 1619 (2014).
 - ²⁴ E. H. H  roz, J. G. Duque, B. Y. Lu, P. Nikolaev, S. Arepalli, R. H. Hauge, S. K. Doorn, and J. Kono, *J. Am. Chem. Soc.* **134**, 4461 (2012).
 - ²⁵ “See supplemental material at [URL inserted by publisher] for additional absorption, RBM, and G-band REP data for characterization of the DGU-generated sample. This material also includes the determination of d-dependence of the REP asymmetries using the third-order model of Ref. 17.”
 - ²⁶ J. Maultzsch, H. Telg, S. Reich, and C. Thomsen, *Phys. Rev. B* **72**, 205438 (2005).
 - ²⁷ C. Fantini, A. Jorio, M. Souza, M. S. Strano, M. S. Dresselhaus, and M. A. Pimenta, *Phys. Rev. Lett.* **93**, 147406 (2004).
 - ²⁸ E. H. H  roz, J. G. Duque, W. D. Rice, C. G. Densmore, J. Kono, and S. K. Doorn, *Phys. Rev. B* **84**, 121403(R) (2011).
 - ²⁹ Y. Wu, J. Maultzsch, E. Knoesel, B. Chandra, M. Huang, M. Y. Sfeir, L. E. Brus, J. Hone, and T. F. Heinz, *Phys. Rev. Lett.* **99**, 027402 (2007).
 - ³⁰ E. Dobard  i  , I. Milo  evi  , B. Nikoli  , T. Vukovi  , and M. Damnjanovi  , *Phys. Rev. B* **68**, 045408 (2003).
 - ³¹ H. Telg, E. H. H  roz, J. G. Duque, X. Tu, C. Y. Khripin, J. A. Fagan, M. Zheng, J. Kono, and S. K. Doorn, *Phys. Rev. B* **90**, 245422 (2014).
 - ³² A. C. Albrecht, *J. Chem. Phys.* **34**, 1476 (1961).
 - ³³ J. G. Duque, H. Telg, H. Chen, A. K. Swan, A. P. Shreve, X. Tu, M. Zheng, and S. K. Doorn, *Phys. Rev. Lett.* **108**, 117404 (2012).
 - ³⁴ K. Sato, R. Saito, A. R. T. Nugraha, and S. Maruyama, *Chem. Phys. Lett.* **497**, 94 (2010).
 - ³⁵ R. M. Martin and L. M. Falicov, in *Light Scattering in Solids I: Introductory Concepts*, Topics in Applied Physics, Vol. 8, edited by M. Cardona (Springer-Verlag, Berlin, 1983) 2nd ed., pp. 79–145.
 - ³⁶ E. Di Donato, M. Tommasini, C. Castiglioni, and G. Zerbi, *Phys. Rev. B* **74**, 184306 (2006).
 - ³⁷ V. Perebeinos, J. Tersoff, and P. Avouris, *Phys. Rev. Lett.* **94**, 027402 (2005).
 - ³⁸ O. N. Torrens, M. Zheng, and J. M. Kikkawa, *Phys. Rev. Lett.* **101**, 157401 (2008).
 - ³⁹ P. M. Vora, X. Tu, E. J. Mele, M. Zheng, and J. M. Kikkawa, *Phys. Rev. B* **81**, 155123 (2010).
 - ⁴⁰ W. Zhou, T. Sasaki, D. Nakamura, H. Saito, H. Liu, H. Kataura, and S. Takeyama, *Appl. Phys. Lett.* **103**, 233101 (2013).

- ⁴¹ C. D. Spataru, S. Ismail-Beigi, L. X. Benedict, and S. G. Louie, Phys. Rev. Lett. **92**, 077402 (2004).
- ⁴² J. Jiang, R. Saito, G. G. Samsonidze, A. Jorio, S. G. Chou, G. Dresselhaus, and M. S. Dresselhaus, Phys. Rev. B **75**, 035407 (2007).
- ⁴³ J. E. Zucker, A. Pinczuk, and D. S. Chemla, Phys. Rev. B **38**, 4287 (1988).
- ⁴⁴ B. Zhu, K. Huang, and H. Tang, Phys. Rev. B **40**, 6299 (1989).
- ⁴⁵ G. Wen and Y.-C. Chang, Phys. Rev. B **45**, 13562 (1992).
- ⁴⁶ E. Bobkin, A. Knorr, and E. Malic, Phys. Rev. B **85**, 033409 (2012).